11. Silicon Isotope Separation utilizing Infrared Multiphoton Dissociation of Si_2F_6 irradiated with Two-Color CO_2 Laser Light

Atsushi YOKOYAMA, Hironori OHBA, Masashi HASHIMOTO
Department of Materials Science, Tokai Research Establishment, Japan Atomic Energy Research Institute
2-4 Shirakata, Tokai-mura, Naka-gun, Ibaraki 319-1195, Japan

Takeshi ISHII, Akio OHYA
Nuclear Development Corporation, 622-12 Funaishikawa, Tokai-mura, Naka-gun, Ibaraki 319-1111, Japan

Shigeyoshi ARAI
Hill Research, 4-1-6 Roppongi, Minato-ku, Tokyo 106-0032, Japan

Silicon isotope separation has been done by utilizing the Infrared Multiphoton Dissociation (IRMPD) of Si_2F_6 irradiated with two-color CO_2 laser lights. The two-color excitation method improved the separation efficiency keeping the high enrichment factors. For example, 99.74 % of ^{28}Si was obtained at 49.63 % dissociation of Si_2F_6 after the simultaneous irradiation of 200 pulses with 966.23 cm^{-1} photons (0.084 J/cm^2) and 954.55 cm^{-1} photons (0.658 J/cm^2), while 2000 pulses were needed to obtain 99.35 % of ^{28}Si at 35.6 % dissociation in the case of only one-color irradiation at 954.55 cm^{-1} (0.97 J/cm^2).

Keywords: Laser isotope separation, Silicon isotopes, CO_2 laser, Two-color irradiation, Infrared multiphoton dissociation

1. Introduction

Natural silicon contains three stable isotopes; ^{28}Si, ^{29}Si, and ^{30}Si with the abundance ratio of 0.9223:0.0467:0.031. There has recently been much attention to the usage of enriched silicon isotopes in various fields.[1] For example, highly enriched ^{28}Si draw attention in microelectronics field, because a silicon single crystal made of almost pure ^{28}Si (99.85%) shows 60% higher thermal conductivity than that made of natural silicon at room temperature.[2]

Laser isotope separation is an attractive separation method, because much higher enrichment factor may be achieved easily in comparison with other methods such as chemical exchange and centrifugation methods. Silicon isotope separation based on isotopically selective infrared multiphoton dissociation (IRMPD) of Si_2F_6 is a very attractive separation method[3], because it can easily dissociate at a low laser fluence, which allows the irradiation of molecules under a parallel laser beam condition, and shows high isotopic selectivity, compared with IRMPD of other silicon molecules such as SiF_4.

High dissociation rate at low laser fluence is fundamentally important for practical large scale isotope separation. Although the production of several tens of grams of 99.7% ^{28}Si at a production rate of 2.5 g/h was demonstrated using a TEA CO_2 laser and an gas flow reactor, it is preferred for more economical large

scale separation to improve production rate. The improvement of the production rate is expected to be achieved using two-color irradiation method instead of the one-color irradiation used in the previous studies, as has been reported in the studies for other isotopes[4]. The two-color irradiation consists of two successive excitation processes: At first, the desired isotopic molecules are excited selectively to quasi-continuum states by the irradiation at the nearly resonant frequency of a fundamental mode of the isotopic molecules at very low fluence. Then, the isotopic molecule excited to the quasi-continuum states are dissociated by the irradiation at non-resonant frequency at relatively high fluence. This excitation scheme may improve not only the dissociation rate but also the isotopic selectivity, because the excitation of the undesired isotopic molecules due to the power broadening of the absorption lines at the first excitation stage is suppressed as a result of the excitation at very low fluence. In this paper we will show the preliminary experimental results for the silicon isotope separation using the two-color IRMPD of Si_2F_6.

2. Experiment

Figure 1 shows the experimental arrangement used in this work. Two Torr of Si_2F_6 in a Pyrex glass cell (2cm i.d. and 10cm long) was irradiated by two CO_2 laser lights through NaCl or KBr windows attached to the both ends of the cell. An Lumonics TEA-841 CO_2 laser and a Ushio UGL-TEA-3C CO_2 laser were used as the excitation and dissociation sources, respectively. The laser beams were counter-propagating in the cell after having been collimated through a 1.5 cm diameter iris. The pulse delay between two laser beams was set to 0 μs using a pulse delay generator (Stanford Research DG-535). The pulse shape of both laser beams is a spike of ca. 100 ns followed by a few μs tail. Concentration of Si_2F_6 before and after irradiation was determined from absorbance of the absorption band around 990 cm^{-1} measured with a FT/IR spectrophotometer (JASCO FT/IR-410). Isotopic compositions of Si_2F_6 were determined from mass spectral peaks at m/e=151 ($^{28}Si^{28}SiF_5^+$), 152 ($^{28}Si^{29}SiF_5^+$), and 153 ($^{28}Si^{30}SiF_5^+$) measured by a quadrupole mass spectrometer (ULVAC MSQ-400).

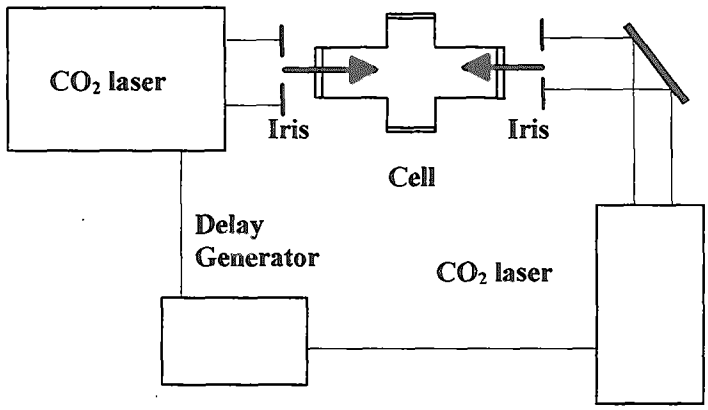

Fig. 1 Experimental arrangement

3. Results and Discussion

Figure 2 shows an IR spectrum of Si_2F_6 from 940 to 1040 cm^{-1}. The absorption peak at 990 cm^{-1} is attributed to anti-symmetric SiF_3 stretching vibration of $^{28}Si^{28}SiF_6$. Naturally Si_2F_6 consists of $^{28}Si^{28}SiF_6$ (85.1%), $^{28}Si^{29}SiF_6$ (8.6%), $^{28}Si^{30}SiF_6$ (5.7%), $^{29}Si^{29}SiF_6$ (0.22%), $^{29}Si^{30}SiF_6$ (0.29%), $^{30}Si^{30}SiF_6$ (0.10%). The two anti-symmetric SiF_3 stretching mode frequencies for these isotopic molecules were calculated by an *ab initio* MO theory at B3LYP/6-31+G(d, p) level of theory using a Gaussian 98 package[5] and

tabulated in Table 1 along with the experimental values. Table 1 also includes the frequencies scaled with the scaling factors determined from the comparison with the experimental values and the calculated IR intensities. In the previous works with one-color irradiation of Si_2F_6 at the fluence of several hundred J/cm^2, maximum enrichment factors were obtained around 950 -955 cm^{-1}, where the absorbance of natural Si_2F_6 is very low. When the higher frequencies were employed, the enrichment factors decreased because of unwished dissociation of $^{28}Si^{28}SiF_6$ due to power broadening of the absorption line. On the other hand, the excitation of Si_2F_6 containing ^{29}Si and/or ^{30}Si at the near resonant frequencies at very low fluence is expected to keep the isotopic selectivity. Therefore, we dissociated Si_2F_6 by the two-color excitation scheme where Si_2F_6 was excited at 966.23 cm^{-1} (10R(6)-line) at fluence below 0.1 J/cm^2 followed by the dissociation of the excited Si_2F_6 at 954.55 cm^{-1} (10P(8)-line) at about 0.8 J/cm^2.

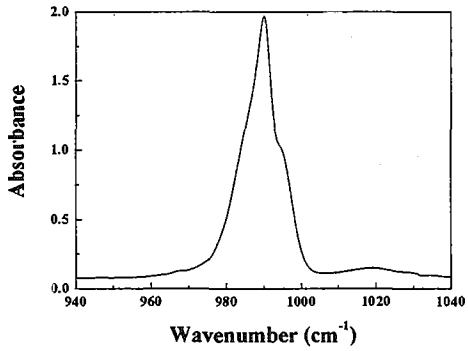

Fig. 2 IR spectrum of natural Si_2F_6 from 940 to 1040 cm^{-1}.

Table 1. Fundamental frequencies (cm^{-1}) for the two anti-symmetric SiF_3 stretching modes of isotopic Si_2F_6 molecules.

Si_2F_6	Calculated	Scaled	IR Intensity	Observed[a)]
$^{28}Si^{28}SiF_6$	961.2	992.3	367.1	992.3
$^{28}Si^{29}SiF_6$	958.3	989.3	335.8	988.4
$^{28}Si^{30}SiF_6$	957.1	988.0	296.2	
$^{29}Si^{29}SiF_6$	953.1	983.9	358.5	
$^{29}Si^{30}SiF_6$	950.3	981.0	330.9	
$^{30}Si^{30}SiF_6$	945.5	976.0	350.4	
$^{28}Si^{28}SiF_6$	948.4	979.0	0.0	979
$^{28}Si^{29}SiF_6$	943.2	973.5	27.0	
$^{28}Si^{30}SiF_6$	936.8	966.9	62.7	
$^{29}Si^{29}SiF_6$	940.3	970.5	0.0	
$^{29}Si^{30}SiF_6$	935.4	965.4	23.6	
$^{30}Si^{30}SiF_6$	932.7	962.5	0.0	

a) reference 6

Dissociation of Si_2F_6 occurs through the following reaction:

$$Si_2F_6 \rightarrow SiF_4 + SiF_2 \qquad E = 44.8 \text{ kcal/mol} \qquad (1)$$

This reaction proceeds through the three-center transition state shown in Fig. 3. The activation energy and the transition state were also calculated at B3LYP/6-31+G(d, p) level of theory. The SiF_2 products are then polymerized to white solids. When the Si_2F_6 containing ^{29}Si and/or ^{30}Si is selectively dissociates, ^{29}Si and/or ^{30}Si are enriched in the products, and ^{28}Si is enriched in the residual Si_2F_6.

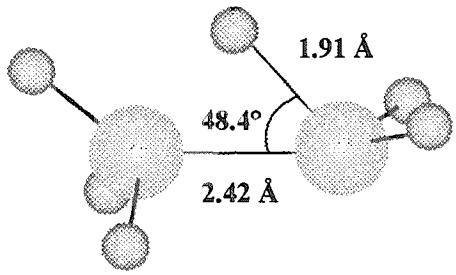

Fig. 3 Transition state structure for reaction (1)

Some results for the silicon isotope separation using one- or two-color irradiation are tabulated in Table 2 along with experimental conditions. It is obvious that the two-color irradiation reduces remarkably the required number of pulses even at lower laser fluence in comparison with the one-color irradiation.

This is favorable for the practical large-scale isotope separation, because the two-color irradiation scheme gives much higher production rate than the one-color irradiation scheme. The isotopic fractions in the

residual Si_2F_6 are plotted as a function of the dissociation fraction of Si_2F_6 in Fig. 4. To obtain the isotopic purity of ^{28}Si above 99.5 % we need to dissociate about 35 % of Si_2F_6. On the other hand, because the ^{30}Si containing Si_2F_6 dissociate selectively at the small dissociation fraction, we need to dissociate less than 10 % of Si_2F_6 to obtain the high ^{30}Si enriched dissociation products. For example, ^{30}Si was enriched to 35 % in the dissociation products, when 7% of Si_2F_6 was dissociated. The high enrichment of both ^{28}Si and ^{30}Si can be attained by two stage of separation processes: At the first stage, the dissociation products is recovered after less than 10 % of Si_2F_6 has been dissociated. Then, the residual Si_2F_6 will be dissociated further to obtain the high enriched ^{28}Si in the residual Si_2F_6. More parameters such as power dependence and laser frequency dependence of the enrichment factors are needed to construct a highly efficient isotope separation process, and further experiments searching the best separation conditions are now in progress.

Table 2 Isotopic fractions in the residual Si_2F_6 after one- or two-color irradiation

Laser Fluence (J/cm^2)		Number of Pulses	Dissociation Fraction (%)	Isotopic Fraction in the residual Si_2F_6(%)		
Excitation Laser	Dissociation Laser			^{28}Si	^{29}Si	^{30}Si
-	0.970	2000	35.6	99.35	0.63	0.02
0.098	0.757	500	34.7	99.5	0.4	0.1
0.098	0.757	1000	46.9	99.86	0.14	0
0.089	0.714	200	49.63	99.74	0.2	0.06
0.084	0.658	200	57.66	99.85	0.1	0.05

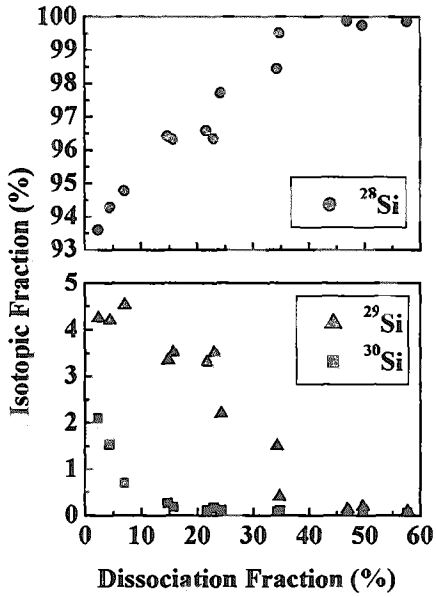

Fig. 4 Dissociation fraction dependence of isotopic fractions in residual Si_2F_6

References

[1] A. Yokoyama, H. Ohba, T. Shibata, S. Kawanishi, S. Sugimoto, T. Ishii, A. Ohya, Y. Miyamoto, S. Isomura, and S. Arai, J. Nucl. Sci. Technol. (submitted) and references therein.

[2] T. Ruf, R. W. Henn, M. Asen-Palmer, E. Gmelin, M. Cardona, H. –J. Pohl, G. G. Devyatych, and P. G. Sennikov, Solid State Comm. **115**, 243 (2000).

[3] K. Tanaka, S. Isomura, H. Kaetsu, Y. Yatsurugi, M. Hashimoto, K. Togashi, and S. Arai, Bull. Chem. Soc. Jpn. **69**, 493 (1996) and references therein.

[4] For example, A. Yokoyama, K. Suzuki, G. Fujisawa, N. Ishikawa and M. Iwasaki, Appl. Phys. **B38**, 99 (1985)

[5] GAUSSIAN 98 (Revision A.3), M. J. Frisch, et al. (Gaussian, Inc., Pittsburgh PA, 1998)

[6] V. Tosa, K. Ashimine, and K. Takeuchi, J. Mol. Struct. **410-411**, 411 (1997).

12. Infrared Photoexcitation Spectroscopy of Conjugated Polymers and Conjugated-Polymer/C_{60} Composites

Yukio FURUKAWA, Ken-ichi KUDO
Department of Chemistry, School of Science and Engineering, Waseda University,
Shinjuku- ku, Tokyo 169-8555, Japan

The processes after photoexcitation in regioregular poly(3-dodecylthiophene) and the composite of regioregular poly(3-dodecylthiophene) and buckminsterfullerene C_{60} have been studied by ultraviolet-visible absorption, fluorescence, and photoexcitation infrared spectroscopy. Photoinduced infrared absorption has been observed by the FT-IR difference-spectrum method, indicating that charge carriers (polarons) of poly(3-dodecylthiophene) are photogenerated. As the C_{60} concentration increases, fluorescence intensity due to poly(3-dodecylthiophene) decreases and simultaneously the intensities of the photoinduced infrared absorption bands increase. The photon-energy dependence of the photoinduced infrared absorption bands is similar to the ultraviolet-visible absorption spectrum of poly(3-dodecylthiophene). These results indicate that electrons are transferred from the excitons in the polymer to C_{60} upon photoexcitation.

Keywords: Conjugated Polymers, Poly(3-dodecylthiophene), Fullerene, Infrared Spectroscopy, Photoexcitation, Electron Transfer

1. Introduction

The supramolecular composite of a conjugated polymer and buckminsterfullerene, C_{60}, exhibits electron transfer from the conjugated polymer to C_{60} after photoexcitation of the conjugated polymer [1-4]. The conjugated polymers such as poly(p-phenylenevinylene) derivatives and polythiophene derivatives are effective donors upon photoexcitation, whereas C_{60} acts as a strong acceptor. The composites and donor/acceptor heterojunctions consisting of a conjugated polymer and C_{60} can be used for photovoltaic devices such as large-area solar cells [5]. Electron transfer or energy transfer from excited states can be studied by fluorescence spectroscopy. Since charge carriers in conjugated polymers, which are expected to be generated from the electron transfer, give rise to giant infrared intensities, infrared spectroscopy is a unique method for probing carriers generated in conjugated polymers. In this paper, we have studied

the photoexcitation processes of the composite of regioregular poly(3-dodecythiophene) (PDT) and C_{60} by using photoexcitation infrared spectroscopy.

2. Experimental

Thin films of PDT and PDT/C_{60} were made by the spin-coating technique on a BaF_2 plate. The C_{60} content per repeating unit of PDT was calculated from the weights of PDT and C_{60}. Photoinduced infrared absorption spectra were measured on a JEOL JIR-5500. A thin film of the sample was set at the head of a liquid-nitrogen cryostat (Oxford DN1754). An aperture (0.435 cm^2) was placed on the sample. Excitation light was incident on this area. Excitation light was provided from an Ar ion laser (Coherent Radiation Innova Model 90-6) and a Xe lamp illuminator. Radiation from a Xe lamp (300 W) was monochromated by a 1/8 m monochromator (Oriel Instruments). The spectral slit width was set at 20 nm. The temperature of the sample was kept at 78 K during the measurement of photoinduced infrared spectra. Photoinduced infrared absorption spectra were obtained by subtracting the light-off spectrum from the light-on spectrum. For the measurement of the action spectrum of photoinduced infrared absorption, the photon flux of the incident light was kept at a constant value 4.38×10^{16} cm^{-2} s^{-1}, which correspond to the power density from 0.97 to 2.1 mW cm^{-2}.

3. Results and Discussion

The ultraviolet-visible and infrared absorption spectra of the PDT/C_{60} composite are the superposition of the bands due to PDT and C_{60}. Thus the interaction between PDT and C_{60} at their ground states is very weak. On the other hand, photoluminescence of PDT is strongly quenched by the addition of C_{60}. This result suggests that energy transfer occurs from the excitons in PDT to C_{60}. The photoinduced infrared spectrum of PDT is shown in Fig. 1 with the spectrum of PDT. The photoinduced infrared spectrum of PDT/C_{60} is almost the same as that of PDT, although the intensity of each of photoinduced band is larger than that of PDT by about one order. The photoinduced infrared spectrum of PDT is attributed to photogenerated carriers (polarons). The observed photoinduced infrared spectra show very complicated features. These features are attributable to the interaction between an electronic transition and vibrational transitions of photogenerated species. No bands due to C_{60}^- are observed in the photoinduced infrared spectrum of PDT/C_{60}. The photoinduced ESR signal due to C_{60}^- is reported [6]. The absorption coefficients of the bands due to C_{60}^- are probably negligibly small, compared with

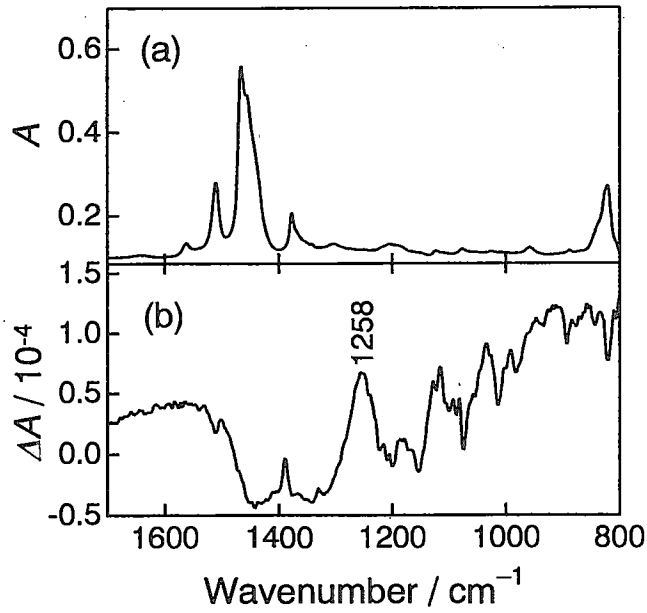

Fig. 1. (a) Infrared and (b) photoinduced infrared absorption spectra of of poly(3-dodecylthiophene).

those of carriers in PDT.

The photon-energy dependence of the 1258-cm^{-1} photoinduced infrared band and the ultraviolet–visible absorption spectrum of PDT are shown in Fig. 2. The observed photon-energy dependence shows a small increase around the electronic absorption edge and a plateau in the region from 2.0 to 2.5 eV, whereas it shows an increase in the region above about 2.5 eV where the electronic absorption of PDT is weak. This result can be explained by considering that the electronic absorption band due to PDT is attributed to the exciton band, and the band gap is located around 2.5 eV. When PDT is irradiated with light whose photon energy is in the region below 2.5 eV, carriers are generated via singlet excitons and/or charge-transfer excitons (polaron pairs). On the other hand, carriers are generated directly, when PDT is irradiated with light whose photon energy is in the region above 2.5 eV. The photon-energy dependence of the 1258-cm^{-1} photoinduced infrared band and the ultraviolet–visible absorption spectrum of PDT/C_{60} composite (C_{60} content, 3.8 mol%) are shown in Fig. 3. The observed action spectrum shows a rapid increase around 2.0 eV, in contrast to the result of PDT. This is because the carriers in PDT is generated via photo-generated excitons in the PDT/C_{60} composite.

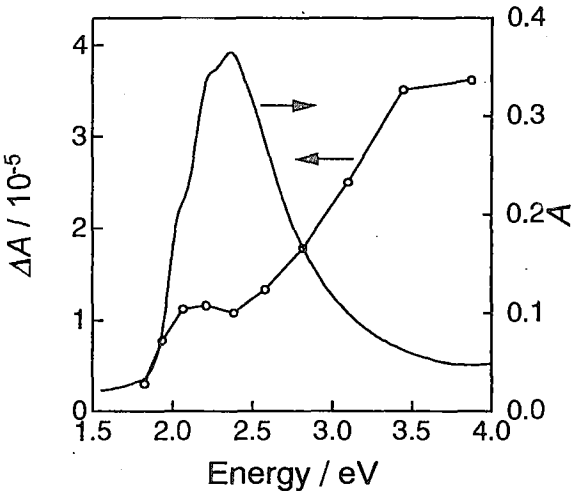

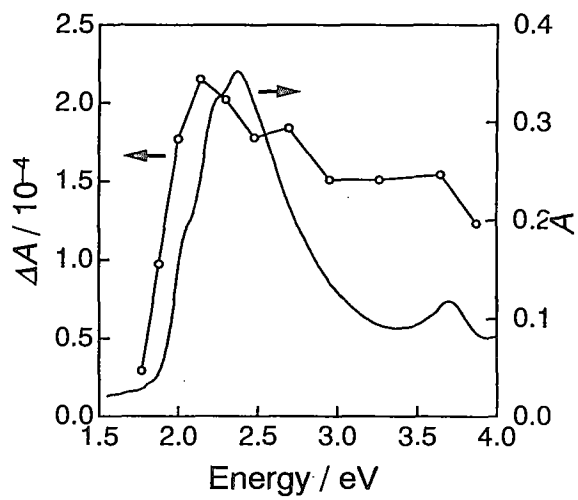

Fig. 2 (left). Photon-energy dependence of the 1258-cm^{-1} photoinduced infrared band and ultraviolet-visible absorption spectrum of poly(3-dodecylthiophene).
Fig. 3 (right). Photon-energy dependence of the 1258-cm^{-1} photoinduced infrared band and ultraviolet-visible absorption spectrum of poly(3-dodecylthiophene)/C_{60} composite. The C_{60} content is 3.8 mol% per repeating unit of poly(3-dodecylthiophene).

4. Conclusions

The electronic absorption band of regioregular poly(3-dodecylthiophene) has been attributed to the exciton band, on the basis of photon-energy dependence of the photoinduced infrared absorption intensity. In the composite with regioregular poly(3-dodecylthiophene) and C_{60}, electrons are transferred from the excitons in the polymer to C_{60} upon photoexcitation. It has been demonstrated that infrared spectroscopy is useful in investigating the charge carriers generated in conjugated polymers.

References

[1] N.S. Sariciftci, L. Smilowitz, A.J. Heeger, F. Wudl, Science, **258**, 1474 (1992).

[2] K. Yoshino, T. Akashi, K. Yoshimoto, M. Yoshida, S. Morita, A.A. Zakhidov, Mol. Cryst. Liq. Cryst., **256**, 343 (1994).

[3] N.S. Sariciftci, A.J. Heeger, Int. J. Mod. Phys. B, **8**, 237 (1994).

[4] N.S. Sariciftci, Prog. Quant. Electr., **19**, 131 (1995).

[5] G. Yu, J. Gao, J.C. Hummelen, F. Wudl, A.J. Heeger, Science, **270**, 1789 (1995).

[6] L. Smilowitz, N.S. Sariciftci, R. Wu, C. Gettinger, A.J. Heeger, and F. Wudl, Phys. Rev. B, **47**, 13835 (1993).

13. 中赤外自由電子レーザーを用いたレーザー生体相互作用研究の展開

Prospect of Laser-tissue Interaction Researches with a Mid-infrared Free Electron Laser

部谷　学，深見裕子，永田博之，粟津邦男
大阪大学大学院工学研究科自由電子レーザー研究施設
573-0128　大阪府枚方市津田山手 2-9-5
Manabu HEYA, Yuko FUKAMI, Hiroyuki NAGATA, and Kunio AWAZU
Institute of Free Electron Laser, Graduate School of Engineering, Osaka University
2-9-5 Tsuda-Yamate, Hirakata, Osaka 573-0128, Japan

Mid-infrared (MIR) light is very suitable for the source of non-invasive bio-molecular surgery because of their high absorption coefficient in bio-tissues. In addition, we can initiate only those interactions of interest, i.e., photothermal, photochemical, and photomechanical interactions, by selectively exciting their corresponding bio-molecular vibration modes. We, however, must control heat diffusion around the irradiated tissues for the realization of non-invasive surgery. A tunable MIR-Free Electron Laser (FEL) has a high repetition rate, which is significantly higher than that for a typical thermal relaxation time of bio-tissues. In order to control thermal and non-thermal effects separately, we need to change the repetition rate of the FEL with the peak power fixed by a micropulse-picking system (MPS). This technique attached to the MIR-FEL system is essential for medical application research using MIR-FELs. The MPS and the prospect of MIR-FEL research are presented.

Key Words: Non-invasive surgery, Heat diffusion, Molecular vibration mode, MIR-FEL, Micropulse-picking.

1．はじめに

レーザーの特徴として単色性・高輝度性・指向性・可干渉性が挙げられる．レーザー治療では病巣部にレーザーを集光することにより，レーザーエネルギーを照射部位に集中的に吸収させ，低侵襲な相互作用を誘起し，非接触で病巣部の治療を行う．あらゆる物質は固有の吸収スペクトルを有しているため，単色な光の励起によって所望の相互作用を選択的に誘起できる．本稿では発振波長可変の中赤外自由電子レーザー（Mid-infrared Free Electron Laser: MIR-FEL）を用いた低侵襲治療法（患者への侵襲（肉体的・精神的負担）を最小限に抑えた治療のこと）の確立のための基礎的研究について述べる．

生体組織との相互作用をレーザー波長という観点から見ると，(1) 紫外・可視域，(2) 近赤外域，(3) 中赤外域に大別できる．(1) 紫外・可視域においては高フォトンエネルギー光による電子遷移が励起される．これらの光は軟組織を高効率にアブレーションできるが，DNA 等への損傷という危険性が常に付きまとう．(2) 近赤外域は生体透過性に優れており，光 CT 等，主に生体表層部における診断技術として期待されている．(3) 中赤外域は高い吸収係数に加え，生体分子の振動領域に対応しており，選択的な相互作用を効率的に誘起できる．近年，低フォトンエネルギーの中赤外光は低侵襲なレーザー医療の光源として注目されつつある．本稿ではこの中赤外光（中赤外域パルスレーザー）に着目する．

中赤外光を用いた低侵襲治療法の実現の鍵は“熱（温度）制御”と“選択的な相互作用の誘起”にある．対象とする治療法によって要求される熱効果の程度は多種多様である．レーザーメスのような生体組織の切開・凝固には“マクロ的”な熱相互作用を，病変部位の局所的な除去には“ミクロ的”な機械的相互作用を利用することが望ましい．照射レーザーのパルス幅を一定とすると，熱効果はパルスの繰り返し周波数（パルス間隔）によって制御できる．一方，選択的な相互作用を誘起するには生体分子種による選択が有効である．即ち，特定の生体分子の分子振動のみを励起することにより，分子レベルでの治療法が期待できる．前述の熱効果制御と組み合わせることによって周辺組織への熱・機械的損傷を最小限に抑えることが可能となる．

本稿では分子振動励起・熱効果制御を同時に達成可能なレーザー光源，MIR-FEL を用いた生体分子手術に関する研究について述べる．2 節では中赤外域におけるレーザー生体相互作用，3 節ではパルス繰り返し周波数（熱）制御のためのパルス切り出し装置について述べ，4 節では MIR-FEL を用いたこれからの研究展開を含め，本稿を総括する．ここでは生体分子手術法を生体分子振動の選択的な励起を用いた治療法と定義する．

2．中赤外域における生体相互作用 [1)]

低侵襲とするためには“熱効果”と“非熱効果”とを分離して考える必要がある．生体組織の主成分は水であるため，一般に両者は中赤外域の水の熱緩和時間“1μs”によって分類される．1μs は単なる指標であり，組織種・変性状態・波長によって熱緩和時間は個々に異なることを注意されたい．本稿では，熱効果は照射部位周辺への熱拡散を伴う相互作用，非熱効果は熱拡散を伴わない相互作用と定義する．

相互作用時間が対象とする生体組織の熱緩和時間よりも短い場合には照射部位周辺への熱拡散は無視できる．この場合，特定の分子振動を熱緩和時間内に励起でき，選択的な現象を引き起こせる．しかしながら，中赤外域の光は熱作用が大きい熱線である．この二面性はパワー密度と相互作用時間（パルス幅と繰り返し周波数 [2)]）に依存している．言いかえるとこれらのパラメーター領域によって 2 つの相互作用に大別できる（図 1）．相互作用は既述した“1μs ルール”によって熱効果と非熱効果に分類される．熱効果には光化学作用と光熱作用がある．熱効果は照射部位周辺への熱拡散を伴うため，マクロ的な相互作用を引き起こす．その反面，過度な熱効果は組織の熱損傷（火傷）に繋がる．一方，非熱効果は光衝撃作用とも呼ばれ，光アブレーション，プラズマ誘起アブレーション，光破壊に分類される．非熱効果では吸収部位における機械的応力が主要因である．熱拡散を伴わないため，相互作用領域を限定できる．ここで相互作用を決めるのはエネルギー密度ではなくパワー密度であることを付記しておく．

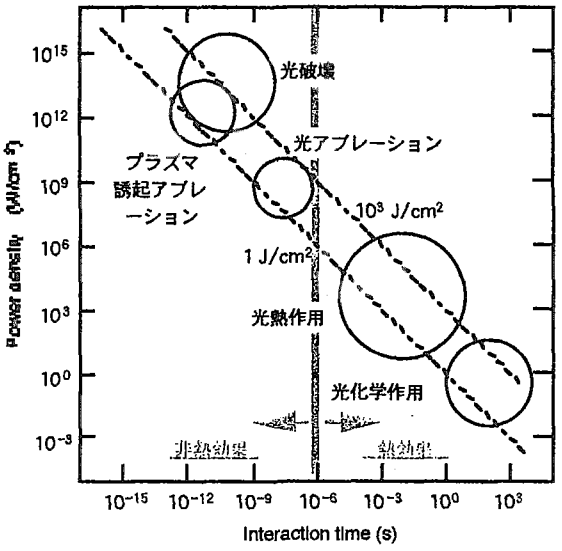

図1　パワー密度（W/cm^2）・相互作用時間（s）とレーザー／生体相互作用．図中にエネルギー密度1，10^3 J/cm^2を点線で示した．

このように，パワー密度と相互作用時間（パルス幅と繰り返し周波数）との組み合わせによ

って種々の治療に適合したレーザー生体相互作用を選ぶことができる．更に，レーザー波長をも任意に設定することによって，より高精度でしかも分子レベルで相互作用を特定できる．これが中赤外域パルスレーザーを用いた生体分子手術法の他に類をみない利点である．

3．中赤外自由電子レーザー装置と繰り返し周波数制御

2 節では分子振動励起・熱制御を同時に実現することが低侵襲な相互作用に繋がることを示した．これには MIR-FEL 発生装置へのマイクロパルス切り出し装置の導入が不可欠である．3.1 では MIR-FEL の特長について，3.2 ではマイクロパルス切り出し装置の原理・原理実証実験について述べる．

3．1．中赤外自由電子レーザー装置 [3)]

中赤外域において生体相互作用は照射レーザーの（1）波長，（2）繰り返し周波数，（3）パワー密度の組み合わせによって決まる．これら 3 つのパラメーターを任意に設定できる唯一の中赤外域パルスレーザーとして MIR-FEL がある．即ち，MIR-FEL の特長として（1）連続的な波長可変性，（2）高ピークパワー（MW 以上），（3）高繰り返し周波数（MHz 以上）が挙げられる．

MIR-FEL では相対論的なエネルギーを持つ電子ビームと電磁場との共鳴的な相互作用によってコヒーレントな電磁波を発生させる．原理の詳細については省略するが，MIR-FEL は加速電子のエネルギーと磁場強度によって発振波長を連続的に変えることができる．他の中赤外域放射光光源と比較してコヒーレントで且つ高輝度（高ピークパワー）である．また，高周波直線加速器を用いた MIR-FEL は高繰り返しのパルス列構造を持つ．

大阪大学大学院工学研究科自由電子レーザー研究施設における MIR-FEL は二重パルス構造（マイクロパルスとマクロパルス）を有している．最小パルス単位はパルス幅約 5-10ps，繰り返し周波数 22.3MHz（パルス間隔 44.8ns）のマイクロパルスである．330 個程度のマイクロパルス群が 1 マクロパルスとして 10Hz で発振している．マクロパルスのパルス幅は約 15μs である．MIR-FEL において熱効果（平均パワー）と非熱効果（ピークパワー）を分離して制御するためには，マクロパルスではなくマイクロパルスの繰り返し周波数を制御する必要がある．

3．2．マイクロパルス切り出し装置 [4,5)]

熱効果と非熱効果を分離して制御するための一手法として，ここではピークパワーを固定して平均パワーのみを変化させる方法を用いる．即ち，マクロパルスから任意の繰り返し周波数でマイクロパルスの切り出しを行う．

図 2 にパルス切り出しの原理図を示す．パルス切り出しには光学音響素子（Acousto-optic modulator: AOM）による光の偏向を用いる．ゲルマニウム（Ge）結晶中に超音波が下から上へ，MIR-FEL が左から右へ伝播する．入射角がブラック角にほぼ一致すると，ブラック回折が起こり，1 次の回折光が観測される．つまり，超音波（粗密波）が任意の時間において反射率の高い鏡面として機能する．この反射率が偏向（切り出し）効率に相当し，原理的には 100%まで達成できる．照射対象が回折（1

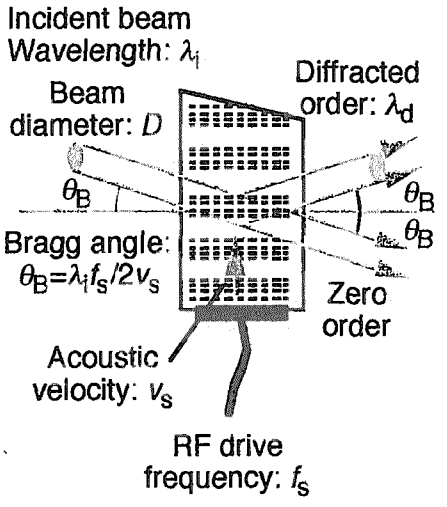

図2　AOMを用いた光の偏向による切り出し原理．

次）光側にあるとすると，超音波の繰り返し周波数を任意に設定することによって切り出しパルス周波数を制御できる（詳細については文献 4 に譲る）．今回開発した切り出し装置では 10 マイクロパルス単位で切り出しを行う．7.5-10.0μm に渡り 50%以上の効率が得られた．また，9.0μm で最大~70%であり，これは仕様値 75%とほぼ一致した．尚，Ge 表面での 50%程度のフレネル反射を考慮に入れていないため，実際の効率は表示値の約 1/2 である．Ge 結晶への入射角度を所望の波長に合わせて調整することにより，この波長依存性を任意の波長域で再現できる．即ち，数個の AOM を並列に用いることによって広範な波長域をカバーできる．

以上のように，MIR-FEL とパルス切り出しとを組み合わせることにより，波長可変範囲 2.0-11.0μm ・ピークパワー数 MW ・平均パワー 0.5-15mW のパラメーター領域において，それぞれを独立に制御できる．この技術は低侵襲生体分子手術の基礎研究にとって必須の基盤技術である．

4．まとめ

生体分子手術の基礎研究において熱・非熱効果を分離するためには，波長可変で高輝度な MIR-FEL の繰り返し周波数制御が重要であることを明らかにした．また，繰り返し周波数を変えるためにパルス切り出し装置を開発し，その有効性を明らかにした．そして，低侵襲な生体相互作用を誘起するレーザーパラメーターの最適化にとってパルス切り出し装置による熱制御が本質的に重要であることを示した．

これからの MIR-FEL 医療応用研究の今後の展望として次の 3 つを考えている．(1) 熱制御によるレーザーパラメーターの最適化．生体軟組織の切除・凝固には蛋白質の変性や熱損傷に注意しなければならない．また，歯牙硬組織の表面改質（再結晶化）においても照射部位の温度が結晶性に強く依存する．(2) 照射中の温度評価．低侵襲プロセスにとって温度の正確な記述は不可欠である．そのためには熱緩和時間よりも速い時間応答での時間分解計測が要求される．著者らは中赤外域においてリュードベルグ原子を用いた高感度な二次元カメラやストリークカメラの導入を計画している．(3) 生体組織の動的光学定数の測定 [6]．照射中の温度変化によって組織の光学定数が変化することは良く知られている．対象とする生体組織の光学定数の温度依存性を定量的に把握することは過度な温度上昇の回避に繋がる．照射中における動的光学定数はレーザー誘起衝撃音の時間波形から導出できる．既に 6μm 帯の水の光学定数を求め，温度上昇に起因すると思われる吸収ピーク波長（変角振動）のレッドシフトを観測している．この技術にパルス切り出し装置・温度計測装置を導入し，様々な組織の動的光学定数のデータベース化を試みる．この技術は照射中の対象組織の変性状態・温度等の実モニタリング技術へも応用できる．

参考文献

1) M. H. Niemz, "Laser-Tissue Interactions", Springer, Ch. 3 (1996).

2) 相互作用時間τ_{int}はパルス幅τ_d，パルス間隔τ_i，露光時間τ_{exp}によって決まる．今，パルス幅が熱緩和時間τ_rよりも十分短い場合を考える．$\tau_i > \tau_r$では$\tau_{int} = \tau_d$，$\tau_i < \tau_r$では$\tau_{int} = \tau_{exp}$となる．

3) T. Tomimasu *et al.*, Nucl. Instr. and Meth. in Phys. Res. B 144, 1 (1998) and references therein.

4) M. Heya *et al.*, SPIE 2001 (to be published).

5) M. Heya *et al.*, Nucl. Instr. and Meth. in Phys. Res. B (submitted).

6) 永田博之ら，レーザー学会第 289 回研究会報告，No. RTM-01-28, 62 (2001)．

14. Growth Dynamics of Single-Wall Carbon Nanotubes and Nanohorn Aggregates Synthesized by CO_2 Laser Vaporization

Fumio KOKAI

Laser Laboratoty, Institute of Research and Innovation
1201 Takada, Kashiwa, Chiba 277-0861, Japan

Abstract

Single-wall carbon nanotubes (SWNTs), 1.2-1.4 nm in diameter, and aggregates of single-wall carbon nanohorns (SWNHs) were synthesized by CO_2 laser vaporization in Ar gas under pressures of 150-760 Torr. At 150 Torr, SWNTs with smaller diameters were synthesized together with amorphous carbon. With an increase in the gas pressure, the yield of SWNTs decreased, the tube diameters increased, and SWNH aggregates were synthesized. At 760 Torr, most of the products were SWNH aggregates. We discuss the temperature-dependent growth of the SWNTs and SWNH aggregates originating in supersaturated carbonaceous vapors confined by Ar gas.

Keywords: **Single-wall carbon nanotube, Carbon nanohorn, Laser vaporization, Growth dynamics**

1. Introduction

CO_2 laser vaporization of pure or metal-containing graphite can synthesize bundles of SWNTs [1,2] and aggregates of single-wall carbon nanohorns (SWNHs) [3]. In contrast to SWNT synthesis using a nanosecond-pulsed YAG laser and a furnace (1200°C) [4], SWNTs were synthesized by the irradiation of continuous-wave [1] and millisecond-pulsed [2] CO_2 laser light at room temperature (RT). By in-situ analysis using video imaging, emission spectroscopy, and shadowgraphy, we suggested that successive ejection of low-velocity hot carbon (mainly C, C_2, and C_3) and metal species from metal-containing graphite plays a critical role in SWNT growth [5,6]. A viscous carbon-metal flow formed mushroom or turbulent-flow-like clouds of condensing clusters and/or particles. The SWNT growth appeared to have originated in the molten carbon-metal particles in the clouds. Recently, the growth of 30-70-nm-long SWNTs in 1 ms was also suggested [7]. However, more detailed understanding of the growth process is needed to enable synthesizing SWNTs with controlled diameters, lengths, bundle structures, etc.

SWNH aggregates with a uniform diameter of ~80 nm appear to consist of tubule-like structures (with a typical diameter of ~2 nm and lengths of 30-50 nm) with conical tips in their outer sides [3]. Unlike a carbon deposit containing cone structures produced from arc discharge, SWNH aggregates can be produced in high yield (95 %) and rate (10 g/h) by CO_2 laser vaporization of pure graphite at RT [3]. Using emission imaging spectroscopy and shadowgraphy, we analyzed significant changes in carbon-species ejection accompanied by a luminous plume, that resulted in condensation of growing clusters and/or particles in a mushroom cloud [8]. We suggested the roles of carbon species with low initial velocities (~$2.2X10^2$ cm/s) and structural rearrangement resulting in graphitic-structure development in the growth of SWNH aggregates composed of graphitic sheaths.

The aim of this study is to further clarify the growth processes of SWNTs and SWNH aggregates. We performed CO_2 laser vaporization of a graphite-Co/Ni (1.2 at.%) target by using a constant laser power density of 30 kW/cm^2, which is suitable for SWNH-aggregate formation. This power density is fairly low compared to those (70-130 kW/cm^2) used for SWNT formation in our previous work [5-7]. So far, several groups have reported the formation of diameter-different SWNTs depending on the type of metal catalysts and furnace temperature. In this work, the formation of diameter-different SWNTs and SWNH aggregates dependent on ambient gas pressure is shown by the measurements of Raman spectra and transmission electron micrographs (TEM). Based on the expansion behaviors and temperature gradients of laser plumes, as well as our previous results of shadowgraphy [6], we discuss temperature-dependent SWNT and SWNH-aggregate growth in a few milliseconds, in addition to a catalytic role of metal in the SWNT growth.

2. Experimental

The experimental setup used for the SWNT and SWNH-aggregate synthesis and laser-plume analysis was nearly identical to the one used in our previous studies [2,5-7,8]. For the synthesis, we used CO_2 laser beams (10.6 μm and 1 kW peak power) with a pulse duration of 20 ms. A rotating graphite-Co/Ni (1.2 at.%) target mounted in a quartz-glass tube was irradiated at a repetition rate of 1 Hz for 10 s at RT. The diameter of the laser spot on the target surface was set to be 1 mm, and a constant laser power density of 30 kW/cm^2 was

used. Ar gas flowed (0.5 l/min) through the glass tube, and its pressure was maintained at 150-760 Torr. Soot-like carbonaceous deposits formed on the quartz plates in front of the graphite-Co/Ni target were characterized by using Raman scattering spectroscopy (excitation wavelength=514.5 nm) and TEM.

During the laser irradiation, we measured the images of the luminous laser plumes rising from the target by using a high-speed video camera with a temporal resolution of 1.67 ms. Temporally and spatially resolved emission spectra of the plumes were also measured by a gated intensified CCD camera (gate width=10 μs) combined with a monochromator. All the spectra were intensity-calibrated using a standard lamp.

3. Results and Discussion

Figure 1a shows examples of the Raman spectra of the soot-like deposits obtained by CO_2 laser irradiation at Ar gas pressures of 150 and 760 Torr. The Raman spectrum at 150 Torr, consisting of a sharp peak at 1594 cm^{-1} (due to the tangential C-C stretching mode) and two broad peaks at 1100-1650 cm^{-1} (due to amorphous carbon) in the high-frequency region, is a typical one for soot-like material containing SWNTs. In the low-frequency region, there is a band characteristic of SWNTs at around 188 cm^{-1} due to the radial breathing mode. With an increase in the Ar gas pressure, the intensities of Raman bands of SWNTs decreased. Fig. 1a also shows the Raman spectrum of a deposit at 760 Torr. A peak at 1340 cm^{-1} with an intensity similar to that of the peak at 1588 cm^{-1}, which is a characteristic of SWNH aggregates [3], is observed. The peak of the radial breathing mode could no longer be observed.

In addition to the decrease in the yield of SWNTs at higher Ar gas pressures, the diameters of the SWNTs varied. Figure 1b shows a series of Raman spectra (100-250 cm^{-1} region) of the deposits produced at different Ar gas pressures. When the Ar gas pressure is increased to up to 550 Torr, radial-breathing-mode peaks appear in the lower frequency region, indicating the presence of larger diameter SWNTs. The positions of the peaks at 188 cm^{-1} at 150 Torr and at 165 cm^{-1} at 550 Torr correspond to the tube diameters of 1.2 and 1.4 nm, respectively.

We investigated the deposits obtained at Ar gas pressures of 150 and 760 Torr by TEM. For the deposit at 150 Torr, bundled and individual SWNTs, including one as short as ~20 nm, were observed. The maximum length of SWNTs was about 200 nm. The TEM micrographs for various places at the deposits obtained at 150 Torr showed that ~5 % of the SWNTs existed with amorphous carbon. Alternatively, SWNH aggregates were observed as in our previous study [3]. Although Co/Ni particles existed together with amorphous carbon, SWNTs were not observed. At 760 Torr, irrespective of the presence of Co/Ni particles (1.2 at.%), most of the deposits were SWNH aggregates.

Figure 2 shows video images of luminous laser plumes observed at various delay times after the start of the laser irradiation at Ar gas pressures of 150 and 760 Torr. As the delay time increases, the laser plumes

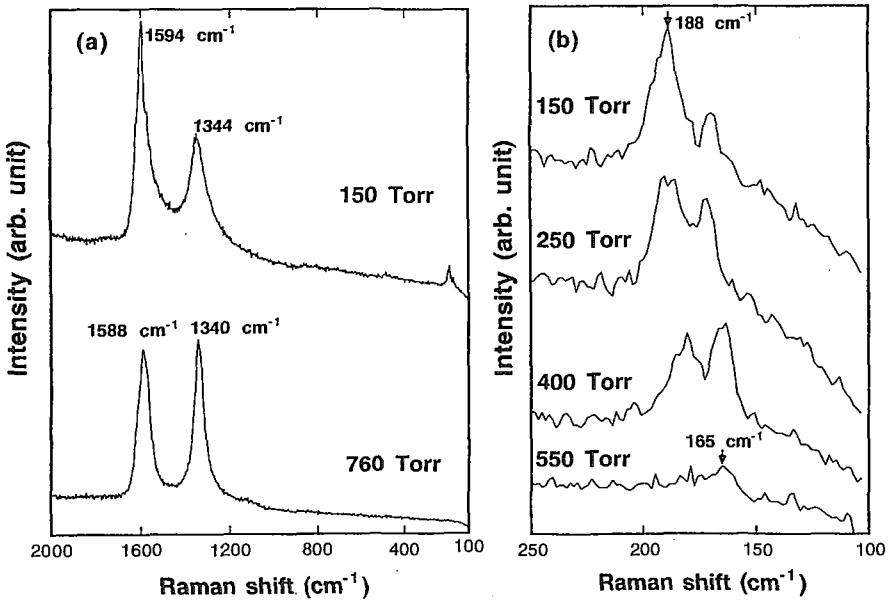

Fig. 1. Raman spectra at (a) 100-2000 and (b) 100-250 cm^{-1} of soot-like deposits produced by CO_2 laser vaporization at RT at Ar gas pressures of 150-760 Torr.

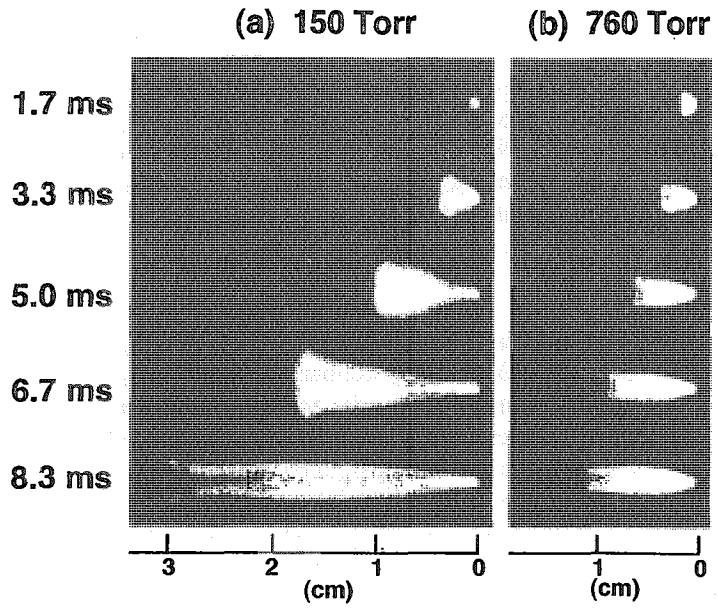

Fig. 2. Video images of laser plumes at different delay times from the start of laser irradiation at Ar gas pressures of (a) 150 and (b) 760 Torr.

become longer. At 150 Torr, plumes are found in wider regions, in particular, near the front edges of the plumes at 3.3, 5.0, and 6.7 ms. After 8.3 ms until the end of laser irradiation (20 ms), plumes similar to those observed at 8.3 ms appeared at 150 and 760 Torr. The evolution of the volumes of the plumes observed earlier at times of up to 8.3 ms appears to be a result of the heating and decomposition processes of the graphite-Co/Ni target surface, which occur with the thermal diffusion of the entire target. After a while, the temperature of the target surface reaches a steady state. When the target was irradiated continuously, the quasi-stationary ejection of carbon species with luminous plumes persisted for a time nearly equal to the laser-pulse duration, as described in our previous report [5,6]. The expanding velocities of the plumes at 150, 400, and 760 Torr were estimated to be 1.1-3.8, 1.0-3.2, and 1.0-2.0 mm/ms from the positions of the edges at 1.7-5.0 ms.

The plume-emission consisted of C_2 (Swan band system), C_3 (comet head system), and continuum (300-800 nm) emissions [5-8]. The continuum emission is probably a result of the blackbody radiation of large clusters and/or small particles, although the characteristics of the clusters and/or particles, such as their size distribution and Co and Ni contents, are unclear. From the measurements of the emission spectra of the plumes, we estimated the temperatures of the clusters and/or particles by fitting the continuum emission into the Planck blackbody distribution function [5,7]. In Figure 3, the temperature, estimated from the spectra measured around the plume edges in Fig. 3, is plotted as a function of the time from the start of the laser irradiation. The temperature at three pressures gradually decreases from ~4500 to 2600-3200 K. From the temperature gradients in Fig. 3, the rates of the temperature fall are calculated to be 317, 235, and 199 K/ms for 150, 400, and 760 Torr. Because of the confinement of the clusters and/or particles by surrounding Ar gas, collisional heating, resulting from the conversion of kinetic energies of the clusters and/or particles into thermal energies, appears to play an important role in preventing the temperature from quick falling.

As the clusters and/or particles collided with Ar atoms, they cooled further, and their kinetic energies dissipated, which finally resulted in the formation of mushroom or turbulent-flow-like clouds [6] due to their rebounding and vortex motions near the edges of the plumes. In the shadowgraph images of the clouds propagating forward, the blackened areas increased due to the more intense light scattering of the condensing materials. We believe that SWNTs and SWNH aggregates are generated in the clouds gradually cooled to RT.

Judging from the SWNT synthesis at different furnace temperatures ranging from 780 to 1460°C, the observed change in tube diameter here is most likely a result from the SWNT-growth fields at different temperatures. For the growth of SWNTs, we think that molten carbon-metal-composite particles formed in supersaturated vapor act as bases for nucleation and growth of SWNTs [5-7]. In the composite particles, Co/Ni particles with nm-size protrusions or certain faces seem to play a crucial role in the segregation of carbon. The change in the tube diameter could be a result of the amount of segregation of

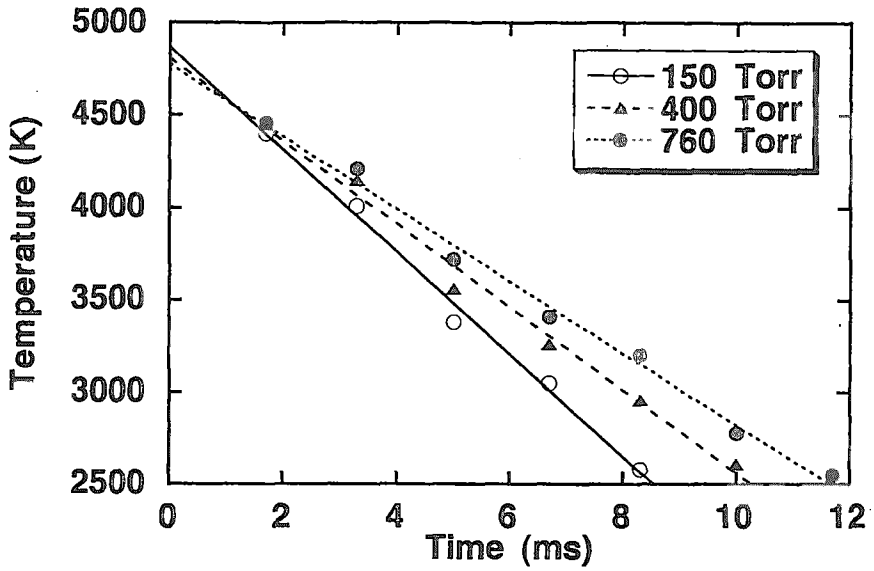

Fig. 3. Estimated blackbody temperatures as a function of time at Ar gas pressures of 150, 400, and 760 Torr.

carbon from the composite particles at different temperatures. We can deduce that this segregation process is governed by such factors as the mobility of carbon and the degree of carbon supersaturation in Co/Ni particles. By assuming the decrease in the temperature of mushroom or turbulent-flow-like clouds similar to that in Fig. 3, the times available for the growth of SWNTs are estimated to be 1.9-2.6 ms (at 150-400 Torr) for the SWNTs (assuming 1400-800°C).

Studies of ~80-nm SWNH-aggregate decomposition in vacuum showed that SWNH aggregates are stable at temperatures of up to at least 1800°C in vacuum [3]. A smaller mushroom cloud was observed at 760 Torr [9], which is a suitable pressure for the formation of SWNH aggregates. The smaller volume of the cloud formed from slowly moving carbon (1-2 mm/ms) suggests the presence of clusters and particles with a higher density. From carbon vapor via liquid-like phase, condensation to solid SWNH aggregates is thought to occur at higher temperatures than those suitable for the growth of SWNTs. At the initial stage of the SWNH-aggregate formation, carbon clusters and small particles formed in plume at temperature of >2500 K may assemble into larger particles with sizes of 30-50 nm, which act as a base of SWNH aggregates, through many-body collisions. Further collisions of the 30-50-nm particles with clusters and small particles could nucleate cone structures in their outer sides. When such growing particles are maintained at high temperature, short graphitic tubule-like structures with lengths of 30-50 nm composed of ~10^4 carbon atoms, may be finally generated through structural rearrangement. Similar to the SWNT, the times available for the growth of SWNH aggregates at 760 Torr are estimated to be 4.0 ms (assuming 2200-1400°C). By consuming carbon vapor at the higher temperature for the SWNH-aggregate formation, even if the temperature fall of the mushroom cloud occurs, carbon vapor could no longer form the growth field for SWNTs to maintain supersaturation and segregation.

References

[1] W.K. Maser, E. Munoz, A.M. Benito, M.T. Martinez, G.F. de la Fuente, Y. Maniette, E. Anglaret , J.-L. Sauvajol, Chem. Phys. Lett. **292**, 587 (1998).
[2] M. Yudasaka, F. Kokai, K. Takahashi, R. Yamada, N. Sensui, T. Ichihashi, S. Iijima, J. Phys. Chem. B **103**, 3576 (1999).
[3] S. Iijima, M. Yudasaka, R. Yamada, S. Bandow, K. Suenaga, F. Kokai, K. Takahashi, Chem. Phys. Lett. **307**, 165 (1999).
[4] T. Guo, P. Nikolaev, A. Thess, D.T. Colbert, R.E. Smalley, Chem. Phys. Lett. **236**, 419 (1995) .
[5] F. Kokai, K. Takahashi, M. Yudasaka, R. Yamada, T. Ichihashi, S. Iijima, J. Phys. Chem. B **103**, 4346 (1999).
[6] F. Kokai, K. Takahashi, M. Yudasaka, S. Iijima, J. Phys. D: Appl. Phys. **33**, 545 (2000).
[7] F. Kokai, K. Takahashi, D. Kasuya, T. Ichihashi, M. Yudasaka, S. Iijima, Chem. Phys. Lett. **332**, 449 (2000).
[8] F. Kokai, K. Takahashi, M. Yudasaka, S. Iijima, J . Phys. Chem. **103**, 8686 (1999).

15. Summary

Toshihiko YAMAUCHI (JAERI)

In the afternoon secession, seven talks including an invited talk on the behavior of molecules in intense laser light field by Prof. Yamanouchi in Tokyo University were presented. The talks about the extraction of positron in the laser light field 10^{27} W/cm^2 and the break of molecule got the great concern of 50 participants. Their seven talks are the topics associated with the decomposition of dioxin analogues (main points in talk and discussions.: comparison of decomposition efficiency on wavelengths by CO_2 laser and FEL and 90 % decomposition efficiency of PCB at JAERI), the isotope separation of silicon (three times improvement of dissociation by the additional FEL irradiation and the 10 %/min dissociation efficiency at Sci. Univ. of Tokyo, and achievement of 99.74 % ^{28}Si and 49.63 % dissociation of Si_2F_6 by two-color CO_2 laser at JAERI), C_{60} etc. (transfer from the excitons in the polymer to C_{60} upon photoexcitation in the composite at Waseda Univ.), carbon nanotube and nanohorn (laser ablation study by ruby laser at JAERI, and the 5 g/10 min carbon nanohorn synthesized by the 3 kW CO_2 laser at Inst. of Res. and Innovation) as a physical and a chemical application, and the tissue renovation (change of the repetetion rate of FEL by a micropulse-picking system (MOPS) at Osaka Univ.) as a medical application. This is the effective photo-reaction obtained by tuning the wavelength which is the main characteristics of FEL.

As mentioned in the workshop by Yamauchi, the bulk chemical reactions as the application of FEL are proposed. This includes the environmental chemistry (NOx etc.), the isotope separation (^{28}Si) and nano-technology (carbon nanotube etc.). Therefore, it is understood that the contents of workshop on FEL application is extremely useful for our coming laser experiments. Anyway, our proposal should be proceeded using the unique characteristics of the very high laser power and the femto-second pulse width.

As FEL system becomes convenient to use for the compact and the easy maintenance, the application study of FEL is getting to be popular here and there. The high power FEL in JAERI and the convenient FELs for the application in Science University of Tokyo, Osaka University and Nihon University will be used on the basis of each laser characteristics. The application of FEL will be expected to contribute to the global social culture.

国際単位系（SI）と換算表

表1　SI基本単位および補助単位

量	名称	記号
長さ	メートル	m
質量	キログラム	kg
時間	秒	s
電流	アンペア	A
熱力学温度	ケルビン	K
物質量	モル	mol
光度	カンデラ	cd
平面角	ラジアン	rad
立体角	ステラジアン	sr

表2　SIと併用される単位

名称	記号
分，時，日	min，h，d
度，分，秒	°，′，″
リットル	l，L
トン	t
電子ボルト	eV
原子質量単位	u

1 eV=1.60218×10^{-19}J

1 u=1.66054×10^{-27}kg

表5　SI接頭語

倍数	接頭語	記号
10^{18}	エクサ	E
10^{15}	ペタ	P
10^{12}	テラ	T
10^{9}	ギガ	G
10^{6}	メガ	M
10^{3}	キロ	k
10^{2}	ヘクト	h
10^{1}	デカ	da
10^{-1}	デシ	d
10^{-2}	センチ	c
10^{-3}	ミリ	m
10^{-6}	マイクロ	μ
10^{-9}	ナノ	n
10^{-12}	ピコ	p
10^{-15}	フェムト	f
10^{-18}	アト	a

表3　固有の名称をもつSI組立単位

量	名称	記号	他のSI単位による表現
周波数	ヘルツ	Hz	s^{-1}
力	ニュートン	N	m·kg/s^2
圧力，応力	パスカル	Pa	N/m^2
エネルギー,仕事,熱量	ジュール	J	N·m
工率，放射束	ワット	W	J/s
電気量，電荷	クーロン	C	A·s
電位，電圧，起電力	ボルト	V	W/A
静電容量	ファラド	F	C/V
電気抵抗	オーム	Ω	V/A
コンダクタンス	ジーメンス	S	A/V
磁束	ウェーバ	Wb	V·s
磁束密度	テスラ	T	Wb/m^2
インダクタンス	ヘンリー	H	Wb/A
セルシウス温度	セルシウス度	℃	
光束	ルーメン	lm	cd·sr
照度	ルクス	lx	lm/m^2
放射能	ベクレル	Bq	s^{-1}
吸収線量	グレイ	Gy	J/kg
線量等量	シーベルト	Sv	J/kg

表4　SIと共に暫定的に維持される単位

名称	記号
オングストローム	Å
バーン	b
バール	bar
ガル	Gal
キュリー	Ci
レントゲン	R
ラド	rad
レム	rem

1 Å=0.1nm=10^{-10}m

1 b=100fm^2=10^{-28}m^2

1 bar=0.1MPa=10^5Pa

1 Gal=1cm/s^2=10^{-2}m/s^2

1 Ci=3.7×10^{10}Bq

1 R=2.58×10^{-4}C/kg

1 rad=1cGy=10^{-2}Gy

1 rem=1cSv=10^{-2}Sv

（注）

1．表1－5は「国際単位系」第5版，国際度量衡局 1985年刊行による。ただし，1 eVおよび1 uの値はCODATAの1986年推奨値によった。

2．表4には海里，ノット，アール，ヘクタールも含まれているが日常の単位なのでここでは省略した。

3．barは，JISでは流体の圧力を表わす場合に限り表2のカテゴリーに分類されている。

4．EC閣僚理事会指令ではbar，barnおよび「血圧の単位」mmHgを表2のカテゴリーに入れている。

換算表

力	N(=10^5dyn)	kgf	lbf
	1	0.101972	0.224809
	9.80665	1	2.20462
	4.44822	0.453592	1

粘度　1 Pa·s(N·s/m^2)=10 P(ポアズ)(g/(cm·s))

動粘度　1 m^2/s=10^4St(ストークス)(cm^2/s)

圧力	MPa(=10bar)	kgf/cm^2	atm	mmHg(Torr)	lbf/in^2(psi)
	1	10.1972	9.86923	7.50062×10^3	145.038
	0.0980665	1	0.967841	735.559	14.2233
	0.101325	1.03323	1	760	14.6959
	1.33322×10^{-4}	1.35951×10^{-3}	1.31579×10^{-3}	1	1.93368×10^{-2}
	6.89476×10^{-3}	7.03070×10^{-2}	6.80460×10^{-2}	51.7149	1

エネルギー・仕事・熱量	J(=10^7 erg)	kgf·m	kW·h	cal(計量法)	Btu	ft·lbf	eV
	1	0.101972	2.77778×10^{-7}	0.238889	9.47813×10^{-4}	0.737562	6.24150×10^{18}
	9.80665	1	2.72407×10^{-6}	2.34270	9.29487×10^{-3}	7.23301	6.12082×10^{19}
	3.6×10^6	3.67098×10^5	1	8.59999×10^5	3412.13	2.65522×10^6	2.24694×10^{25}
	4.18605	0.426858	1.16279×10^{-6}	1	3.96759×10^{-3}	3.08747	2.61272×10^{19}
	1055.06	107.586	2.93072×10^{-4}	252.042	1	778.172	6.58515×10^{21}
	1.35582	0.138255	3.76616×10^{-7}	0.323890	1.28506×10^{-3}	1	8.46233×10^{18}
	1.60218×10^{-19}	1.63377×10^{-20}	4.45050×10^{-26}	3.82743×10^{-20}	1.51857×10^{-22}	1.18171×10^{-19}	1

1 cal= 4.18605J（計量法）

= 4.184J（熱化学）

= 4.1855J（15℃）

= 4.1868J（国際蒸気表）

仕事率　1 PS(仏馬力)

= 75 kgf·m/s

= 735.499W

放射能	Bq	Ci
	1	2.70270×10^{-11}
	3.7×10^{10}	1

吸収線量	Gy	rad
	1	100
	0.01	1

照射線量	C/kg	R
	1	3876
	2.58×10^{-4}	1

線量当量	Sv	rem
	1	100
	0.01	1

（86年12月26日現在）